# Creep-free polyelectrolyte elastomer for drift-free iontronic sensing

Yunfeng He [1,3], Yu Cheng[2,3], Canhui Yang [1] ✉ & Chuan Fei Guo [2] ✉

Artificial pressure sensors often use soft materials to achieve skin-like softness, but the viscoelastic creep of soft materials and the ion leakage, specifically for ionic conductors, cause signal drift and inaccurate measurement. Here we report drift-free iontronic sensing by designing and copolymerizing a leakage-free and creep-free polyelectrolyte elastomer containing two types of segments: charged segments having fixed cations to prevent ion leakage and neutral slippery segments with a high crosslink density for low creep. We show that an iontronic sensor using the polyelectrolyte elastomer barely drifts under an ultrahigh static pressure of 500 kPa (close to its Young's modulus), exhibits a drift rate two to three orders of magnitude lower than that of the sensors adopting conventional ionic conductors and enables steady and accurate control for robotic manipulation. Such drift-free iontronic sensing represents a step towards highly accurate sensing in robotics and beyond.

Biological sensory systems have evolved the capability to feel and interact with the surroundings. Artificial haptic technologies based on skin-like sensors are promoting wide applications such as robotic haptics[1–3], automatic pilot and drive[4–6], virtual reality[7–9] and wearable healthcare[10–12]. An ideal sensor for such applications must detect pressure with both high sensitivity and high accuracy. However, the viscoelastic creep of the soft materials causes signal drift and inaccurate measurement under prolonged high stresses[13–15]. Therefore, existing flexible pressure sensors can hardly be used as 'force meters'. A sensory system using such sensors may cause a wrong trigger or safety concerns.

Signal drift is particularly prevalent in iontronic sensors, which are a family of emerging sensing devices with superior sensing properties[16–18]. An iontronic sensor uses a micro-structured soft ionic conductor as the active material. An electric double layer (EDL) with nanoscale charge separation is formed at the ionic conductor–electronic conductor interface[19]. The creep of the ionic conductor caused by molecular rearrangements[20] or the disentanglement of polymer chains[21] changes the contract area of the iontronic interface and leads to signal drift. In addition, an ionic gel is a composite composed of a polymer matrix infiltrated with ionic solvent. Under compression, leakage of the ionic solvent readily occurs because the gel expels solvent to reduce the free energy of mixing[22,23], and the Laplace pressure-induced osmocapillary phase separation pulls liquid out[24]. The leakage expands the effective area of EDL and up-drifts the sensing signal[15]. Thus, an ideal ionic conductor for drift-free iontronic sensors should be both creep-free and leakage-free.

In this Article, we report drift-free iontronic sensing by rationally designing and synthesizing a leakage-free and creep-free polyelectrolyte elastomer at the molecular level. We engraft cations to the polymer backbone to suppress leakage and copolymerize the ionic segments with neutral slippery segments with a high-covalent crosslink density for low creep. The polyelectrolyte elastomer exhibits low creep, no ion leakage and high stretchability. An iontronic sensor using the polyelectrolyte elastomer exhibits an initial drift rate of 0.01–0.1% min⁻¹ at 500 kPa and decreases to 0.001% min⁻¹ within 10 min, two to four orders of magnitude lower than that of sensors adopting other ionic conductors. The signal of the sensor barely drifts under 500 kPa, a pressure comparable to the Young's modulus (~1.12 MPa), for 48 h. The accurate and stable sensing capability of the sensor enables reliable control and manipulation of a robotic gripper.

## Leakage-free and creep-free polyelectrolyte elastomer

The sensor consists of a micro-structured ionic conductor sandwiched between two electronic conductors (Fig. 1a). When the electronic

[1]Shenzhen Key Laboratory of Soft Mechanics and Smart Manufacturing, Department of Mechanics and Aerospace Engineering, Southern University of Science and Technology, Shenzhen, P. R. China. [2]Department of Materials Science and Engineering, Southern University of Science and Technology, Shenzhen, P. R. China. [3]These authors contributed equally: Yunfeng He, Yu Cheng. ✉e-mail: yangch@sustech.edu.cn; guocf@sustech.edu.cn
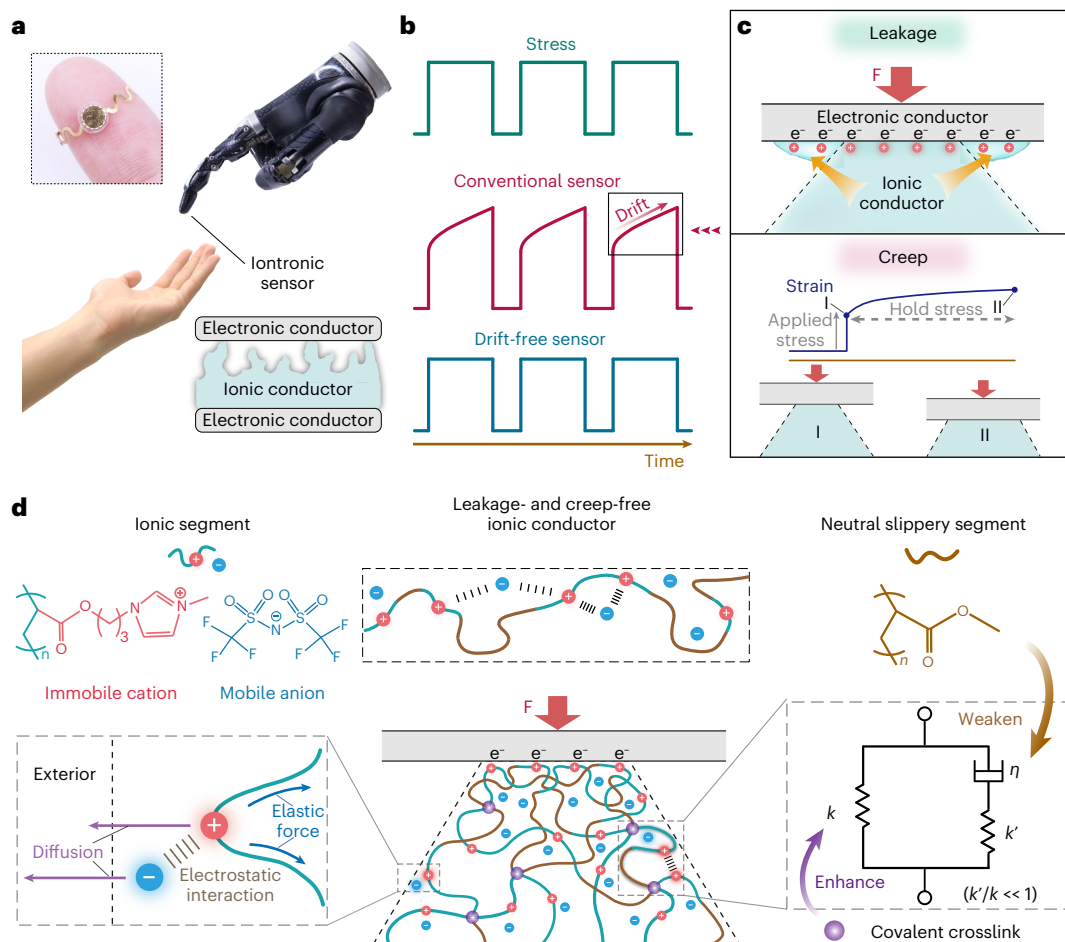
**Fig. 1 | Principles, materials and chemistries for drift-free iontronic sensing. a**, Illustration of an iontronic sensor as an artificial skin for human–machine interactions. The iontronic sensor used in this work consists of a layer of micro-structured ionic conductor sandwiched between two layers of electronic conductors. Top left: The appearance of the sensor, which employs a polyelectrolyte elastomer as the ionic conductor and gold as the electronic conductor. **b**, Subject to a square-wave stress, conventional iontronic sensors generate drifted signals and cause inaccurate sensing, while a drift-free iontronic sensor generates non-drifted signals for accurate sensing. **c**, The signal drift of conventional iontronic sensors is attributed to the leakage of the ingredients and/or the creep of the ionic conductor under prolonged static stress. **d**, Designing principles of a leakage-free and creep-free polyelectrolyte elastomer for drift-free iontronic sensing. The chemical structures of the ionic segment, AMT (top left), and the neutral slippery segment, MA (top right), are illustrated. 'F' in **c** and **d** represents applied force.

conductor contacts the ionic conductor, the electronic charges in the electrode and the ionic charges in the ionic conductor accumulate to form an EDL, for which the capacitance ($C$) value is proportional to the contact area. Conventional iontronic sensors generate drifted signals when subjected to a prolonged high stress, while an ideal iontronic sensor generates non-drifted signals (Fig. 1b). The signal drift of existing iontronic sensors is caused by the leakage of the ingredients and the creep of the ionic conductors (Fig. 1c). Finite element analysis regarding the viscoelastic creep of ionic conductors (Supplementary Note 1) reveals that the contribution of entropic elasticity must far exceed that of viscoelasticity to guarantee creep-free sensing (Supplementary Fig. 1). Note that creep also causes signal drift in other types of flexible sensor.

Here we synthesize a soft ionic conductor that is leakage-free and creep-free to eliminate signal drift (Fig. 1d). We synthesize a random copolymer network consisting of two types of segments: a charged segment and a neutral slippery segment. For leakage-free behaviour, the polymer network contains no solvent and has at least one type of ion (cations in this work) engrafted to the polymer chains. When in contact with other materials, the ion concentration gradient at the iontronic interface facilitates the outward diffusion of ions. However, long-range directional diffusion of ions will stretch the polymer chains, reducing

the number of chain configurations and decreasing the entropy. The decrease in entropy induces an elastic force in the polymer chain to prohibit the outward diffusion of the engrafted ions, as well as the mobile counterions through electrostatic interactions.

A polyelectrolyte elastomer is intrinsically viscoelastic because of the entanglement of polymer chains and the interchain interactions between the charged segments[25]. For creep-free behaviour, neutral slippery segments are copolymerized to weaken viscoelasticity, and a high-covalent crosslink density is used to enhance entropic elasticity. The polyelectrolyte elastomer is considered as a standard linear solid consisting of an elastic spring of stiffness $k$ in parallel with a Maxwell arm, which contains a spring of stiffness $k'$ ($k' \ll k$) and a dashpot of viscosity $\eta$ in series. On one hand, the neutral slippery segments lessen the viscosity by weakening the interchain interactions, that is, reducing $\eta$. On the other hand, increasing the covalent crosslinking density enhances the entropic elasticity, that is, enlarging $k$, by suppressing the fluctuations of polymer chains to a greater extent and increasing the chain density[22]. The polymer network is nearly creep-free when the applied stress is mostly carried by the elastic spring (Supplementary Figs. 2–4).

The design of leakage- and creep-free ionic conductors can be illustrated by various chemistries. Here we synthesize 1-(3-(acryloyloxy)
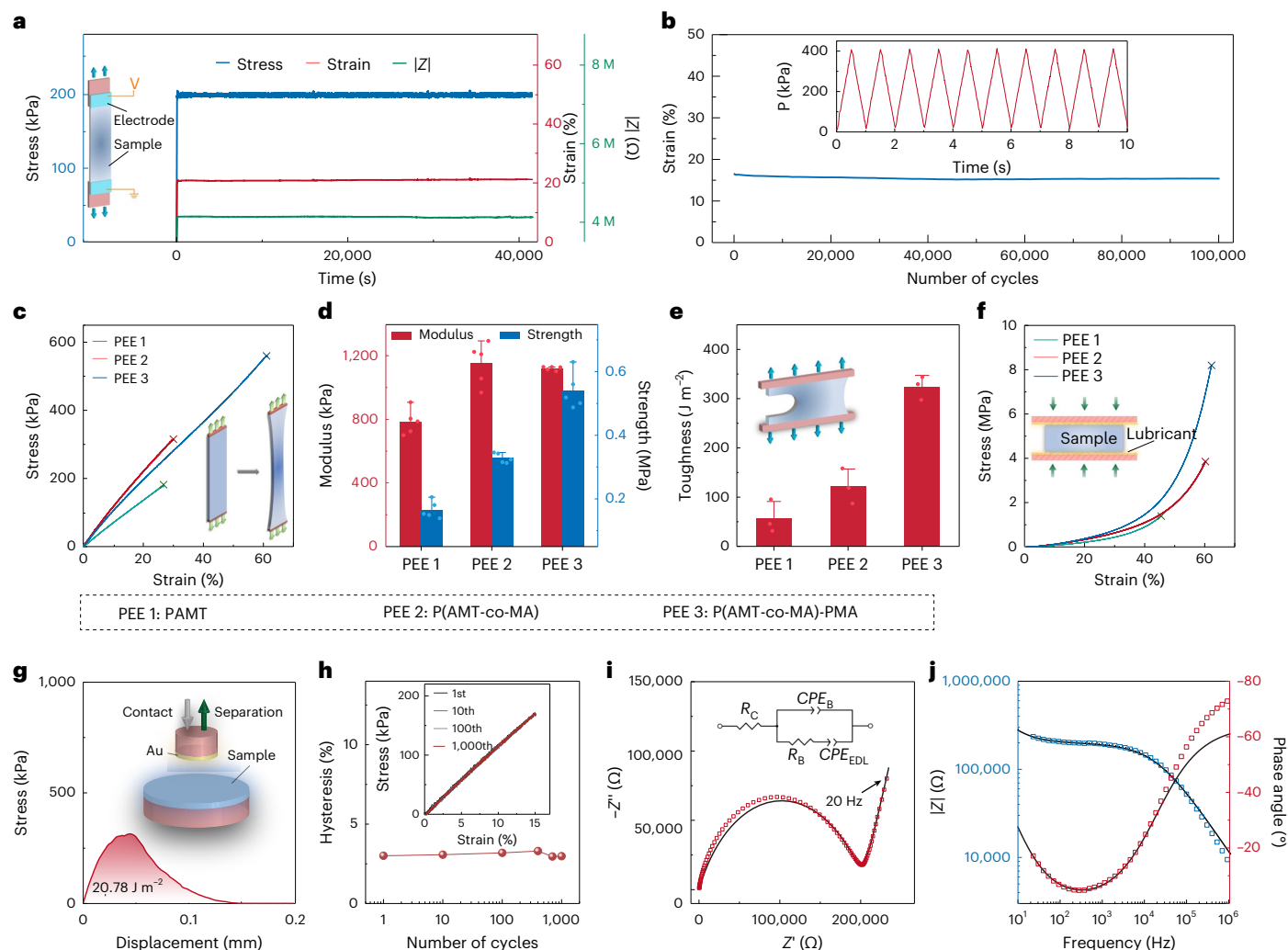
**Fig. 2 | Characterizations of the polyelectrolyte elastomer. a**, The variations of strain and impedance of P(AMT-co-MA)-PMA with time under a constant tensile stress of 200 kPa. **b**, The variation of the peak strain of P(AMT-co-MA)-PMA with time under cyclic tension with a maximum stress of 400 kPa. The inset shows the loading profile. **c**, Uniaxial tensile stress–strain curves of PAMT, P(AMT-co-MA) and P(AMT-co-MA)-PMA. **d**–**f**, Modulus and strength (**d**), toughness (**e**) and uniaxial compressive stress–strain (**f**) curves of the three materials. The data are presented as mean values ± standard deviation. The dots in **d** and **e** represent the raw data. The sample size is $n = 5$ for **d** and $n = 3$ for **e**. **g**, Stress–displacement curve of the tack test between P(AMT-co-MA)-PMA and an Au electrode. **h**, Hysteresis behaviour of P(AMT-co-MA)-PMA at 15% tensile strain over 1,000 loading–unloading cycles. The inset shows the stress–strain curves at the 1st, 10th, 100th and 1,000th cycles. **i,j**, Nyquist plot (**i**) and bode phase plot (**j**) of P(AMT-co-MA)-PMA. The grey lines are theoretical fittings using the equivalent circuit model in the inset of **i**. $R_C$ represents the contact resistance, $R_B$ represents the bulk resistance, $CPE_B$ represents the constant phase element of the bulk and $CPE_{EDL}$ represents the constant phase element of the electric double layer.

propyl)-3-methylimidazolium bis(trifluoromethane)sulfonimide (AMT) as the ionic segment and use methyl acrylate (MA) as the neutral slippery segment to synthesize a network of poly(1-(3-(acryloyloxy)propyl)-3-methylimidazolium bis(trifluoromethane)sulfonimide-co-methyl acrylate) (P(AMT-co-MA)). Because ionic species are generally hygroscopic, we elaborately synthesize AMT with hydrophobic moieties to minimize the complications caused by humidity. The cation of AMT contains a vinyl group, and the P(AMT-co-MA) network contains engrafted cations and mobile anions. The composition and the chemical structure of AMT are validated by $^1$H-nuclear magnetic resonance (NMR) and $^{19}$F-NMR spectroscopy (Supplementary Fig. 5). Diluting AMT with MA mitigates the friction between polymer chains because MA contains a short and low-polarity side chain.

## Characterizations of the polyelectrolyte elastomer

In addition to the leakage-free and creep-free behaviours, other aspects of the polyelectrolyte elastomer are also rationally tailored.

We investigate the effects of crosslinking density and the molar ratio of AMT:MA on the mechanical and electrical properties of P(AMT-co-MA) and further toughen the P(AMT-co-MA) network with physically interpenetrated polymethyl acrylate (PMA) long chains[26] (Supplementary Fig. 6). We set the crosslinker content to be 3 mol%, the molar ratio of AMT:MA to be 1:2 and the content of long-chain PMA to be 10 wt.% for optimized mechanical properties, interfacial adhesion and electrical properties (Supplementary Figs. 7–16). We define the creep-free criterion as less than 1% normalized creep strain under 100 kPa for 10 min. Our experimental results indicate that the co-polymerization plays a dominant role to suppress creep (Supplementary Table 1), while the addition of long-chain PMA mainly contributes to the toughening of the polyelectrolyte elastomer. Fitting the creep data to the standard linear solid model, $k$ increases while $\eta$ decreases with co-polymerization and the value of $k'$ is smaller than $k$ by two orders of magnitude for being creep-free (Supplementary Table 2), which are in line with the finite element analysis results. Further creep tests indicate that the normalized creep strain increases with stress (Supplementary Fig. 17).
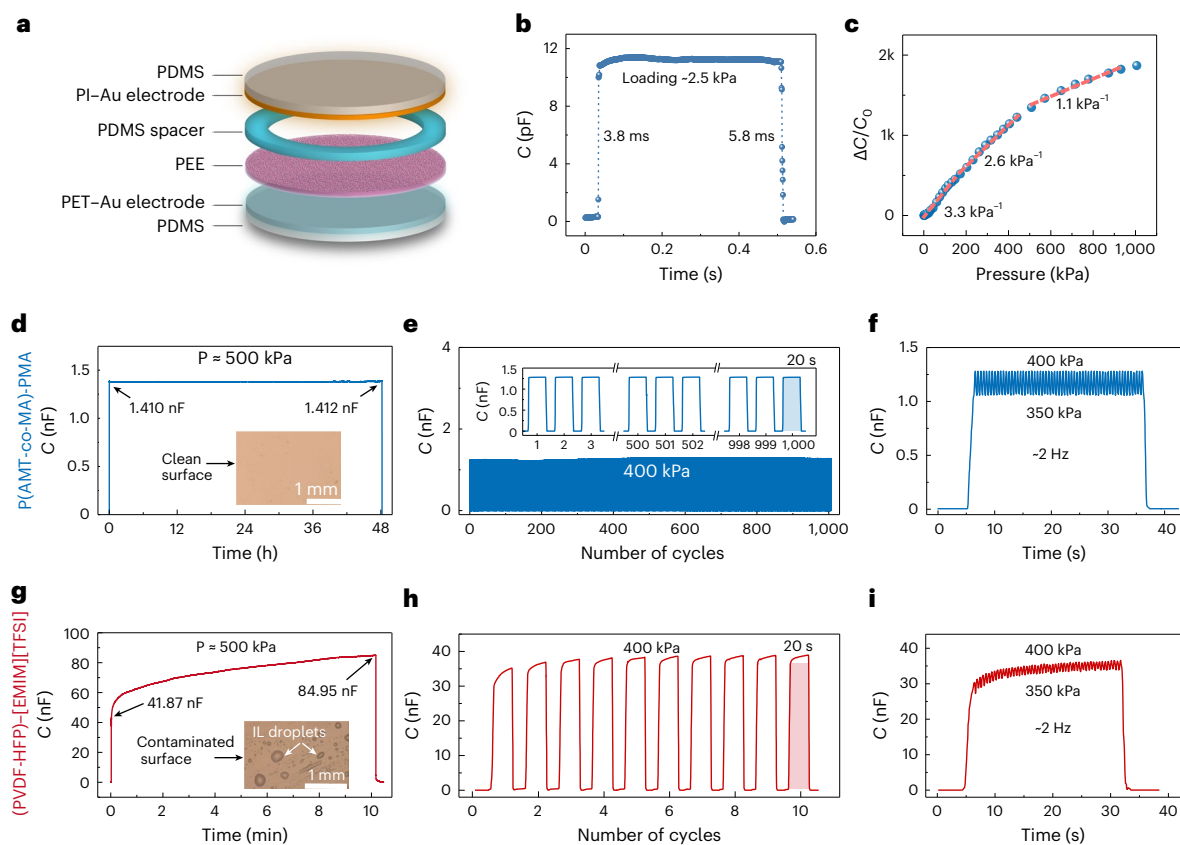
**Fig. 3 | Sensing properties of the iontronic sensor. a**, Schematic of the composition of a PEE-based iontronic sensor. **b**, Response time and recovery time of the sensor. **c**, $\Delta C/C_0$ varies with pressure. **d**, Capacitance of the PEE-based sensor varies with time under static compression of 500 kPa for 48 h. The inset shows the clean surface of the Au electrode after the test. **e**, Cyclic compression of the PEE-based sensor under square waves, each endures for 20 s, over 1,000 cycles at 400 kPa. The inset zooms in on the signals at the initial, middle and final three cycles. **f**, Response of the PEE-based sensor subject to the superposition of static and dynamic loads. The average stress is 375 kPa, and the amplitude and frequency of the fluctuation are 50 kPa and 2 Hz, respectively. **g**, Capacitance of an ionogel-based sensor varies with time under static compression of 500 kPa for 10 min. The inset shows the contaminated surface of the Au electrode after the test. IL, ionic liquid. **h**, Cyclic compression of the ionogel-based sensor under square waves, and each endures for 20 s over 10 cycles at 400 kPa. The solid red bar represents the duration of time, 20 s. **i**, Response of the ionogel-based sensor subject to the same superposition of static and dynamic loads as before.

The polyelectrolyte elastomer P(AMT-co-MA)-PMA is creep-resistant so that the sample maintains its mechanical and electrical properties (for example, tensile strain and impedance) when subject to 200 kPa for 40,000 s (Fig. 2a). The marked creep resistance is also verified under dynamic loads. The peak strain barely changes over 100,000 cycles under a cyclic load of triangular waves with a peak stress of 400 kPa and a frequency of 1 Hz (Fig. 2b). The uniaxial tensile curves of the optimized polyelectrolyte elastomers poly(1-(3-(acryloyloxy) propyl)-3-methylimidazolium bis(trifluoromethane)sulfonimide) (PAMT), P(AMT-co-MA) and P(AMT-co-MA)-PMA, represented by PEE1, PEE2 and PEE3, respectively, are compared in Fig. 2c. The toughened PEE3 possesses the largest fracture strain of 61.3%, the highest tensile strength of 560 kPa (Fig. 2d), the highest fracture energy of 323.5 J m$^{-2}$ (Fig. 2e) and the highest compressive strength of 8.2 MPa (Fig. 2f). Hereafter, we refer to the optimized P(AMT-co-MA)-PMA as PEE for concision unless otherwise specified.

Under dynamic compression, the delayed recovery of sticky and hysteretic ionic conductors engenders a larger capacitance to cause over measurement and should be prevented. PEE has a non-tacky surface and exhibits low hysteresis. The adhesion energy of PEE with gold (Au) is 20.78 J m$^{-2}$ (Fig. 2g), barely impeding the recovery of the sensor (Fig. 3). We examine the hysteresis of PEE by cyclically stretching a sample to 15% strain. Hysteresis is defined as the energy dissipated during one loading cycle divided by the work done by external work during that loading cycle. The stress–strain curves of the 1st and the

1,000th cycles almost overlap, giving an average hysteresis of <3% over 1,000 cycles (Fig. 2h).

The ionic conductivity and charge density of ionic conductors are essential to the functions of iontronic sensors. We conduct ac-impedance measurements and measure the Nyquist plot (Fig. 2i) and the Bode phase plot (Fig. 2j) of PEE, as well as that of PAMT and P(AMT-co-MA; Supplementary Fig. 15). By fitting the impedance data to the equivalent circuit model in Fig. 2i (Supplementary Note 2)[27] using the fitting parameters listed in Supplementary Table 3, the capacitance per unit area between PEE and gold is $2.18 \times 10^5$ pF cm$^{-2}$, and the conductivity of PEE is $2.47 \times 10^{-5}$ S m$^{-1}$, comparable to that of other polyelectrolyte elastomers[28]. PEE has a low glass transition temperature of −6.9 °C (Supplementary Fig. 18a), which facilitates selective ion transport through localized segmental chain motion and ion hopping[29] and is thermally stable up to 350 °C (Supplementary Fig. 18b).

## Sensing properties of the iontronic sensor using PEE

We construct an iontronic sensor by sandwiching a layer of PEE between two layers of gold deposited on polyimide (PI) (Fig. 3a). Introducing microstructures enables high sensitivity over a broad linear range[30]. Here we fabricate graded intrafillable architectures[31] on the top surface of PEE and the top PI–Au electrode to boost the sensitivity and working range (Supplementary Fig. 19) and use a flat polyethylene terephthalate (PET)–Au bilayer as the bottom electrode. A 50-µm-thick polydimethylsiloxane
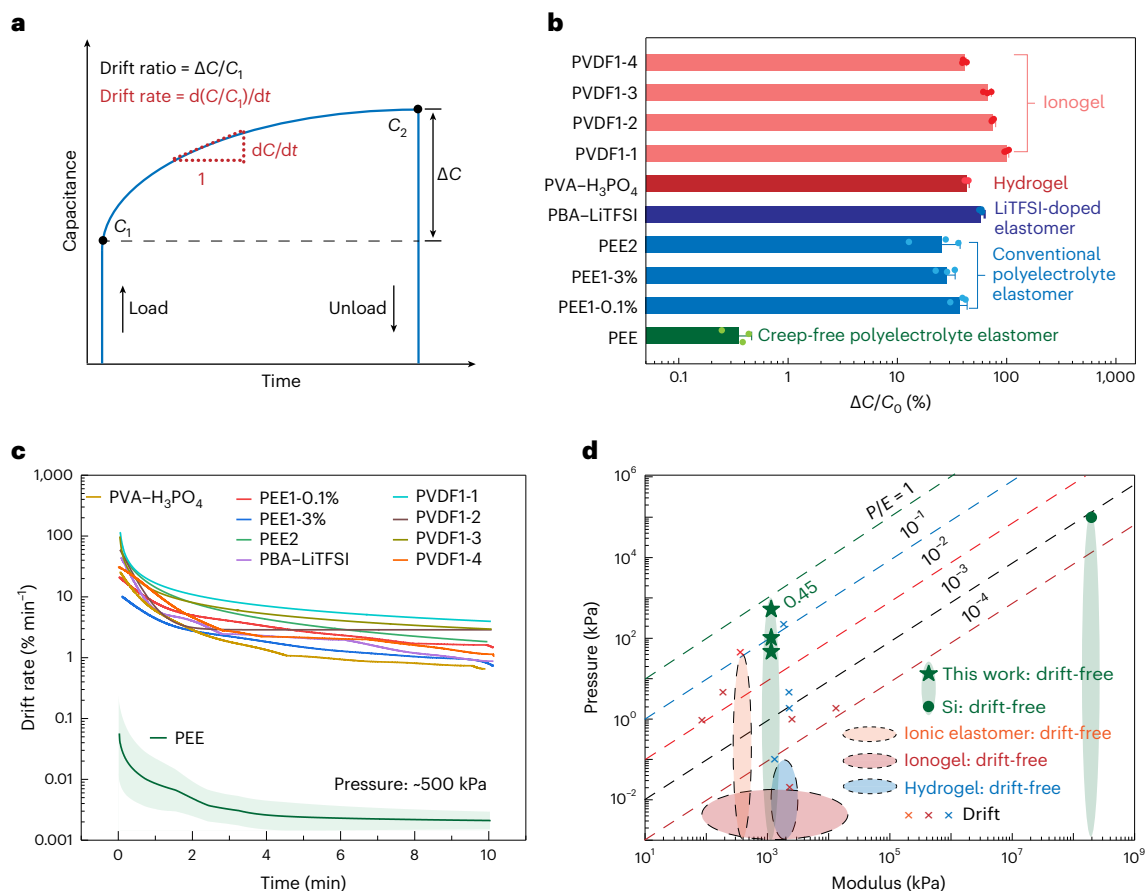
**Fig. 4 | Drift ratio and drift rate of various iontronic sensors. a**, Definition of drift ratio and drift rate. **b**, Comparison of the drift ratios of the sensors based on different ionic conductors under the same pressure (~500 kPa) for 10 min. PEE1-0.1% represents PEE1 with a crosslink density of 0.1%. PVDF1-$x$ represents a mass ratio of 1 to $x$ between PVDF-HFP and the infiltrated ionic liquid [EMIM] [TFSI]. The data are presented as mean values ± standard deviation. The sample size is $n$ = 3. **c**, The variations of drift rate with time for different sensors under a pressure of ~500 kPa. The error band represents standard deviations. The sample size is $n$ = 3. **d**, Pressure–modulus diagram. We define the drift-free criterion as less than 1% drift ratio under a specific pressure for 10 min. The dashed lines represent materials that allow drift-free sensing under different $P/E$ ratios. The regions enclosed by dashed oval curves are conservative estimations for drift-free sensing.

(PDMS) ring is used as a spacer, and two 100-µm-thick PDMS films are used to encapsulate the sensor (Supplementary Fig. 20). The sensor exhibits a response time of ~3.8 ms and a recovery time of ~5.8 ms when subjected to a sudden load of 2.5 kPa (Fig. 3b), and can detect vibration signals up to 80 Hz (Supplementary Fig. 21). The hysteresis of the sensor stabilizes at about 7.6% over 1,000 cycles when subjected to loading–unloading cycles with a peak pressure of 100 kPa (Supplementary Fig. 22). The sensor exhibits a sensitivity of 3.3 kPa$^{-1}$ within 200 kPa, 2.6 kPa$^{-1}$ within 200–500 kPa, and 1.1 kPa$^{-1}$ within 500–1,000 kPa (Fig. 3c). Both the sensitivity and working range are superior to that of most traditional capacitive pressure sensors[14,32–34] (Supplementary Table 4). The sensing performance of the sensors is also highly repeatable (Supplementary Fig. 23). The capacitance changes negligibly as the relative humidity fluctuates between 20% and 96% owing to the hydrophobic nature of PEE (Supplementary Fig. 24). Note that PEE is solution processable and complies with large-scale manufacturing techniques. For example, we used laser cutting to fabricate a PEE-based sensor array with 26 sensors (Supplementary Fig. 25).

Our sensor exhibits negligible signal drift under either long-term high static pressure or cyclic loads with square waves. We apply a static pressure of ~500 kPa to the sensor, and its capacitance maintains ~1.410 nF over 48 h and rapidly recovers to the original value (~1 pF) upon release (Fig. 3d). Microscopic inspection shows that the surface of the PET–Au electrode is clean, indicating no leakage (inset of Fig. 3d). Next, we apply a cyclic load of 400 kPa using square waves, with each

wave enduring for 20 s. The sensor outputs square-wave signals for each cycle over 1,000 cycles (Fig. 3e). The drift-free response is also verified in a more complicated situation – a superposition of static pressure of 375 kPa and dynamic compression with a periodic fluctuation of 50 kPa and a frequency of 2 Hz, and the response of the sensor is in phase with the stimuli (Fig. 3f).

A control sensor using ionogel exhibits substantial signal drift. We use micro-structured 1-ethyl-3-methylimidazolium bis(trifluoromethylsulfonyl)imide ([EMIM][TFSI])-infused poly(vinylidene fluoride-co-hexafluoropropylene) (PVDF-HFP) ionogel, a widely used ionic conductor in iontronic sensors, for comparison. Under a static compression of 500 kPa, the capacitance drifts by ~102.9% within 10 min, and the surface of the PET–Au electrode is contaminated by the leaked ionic liquid (Fig. 3g). The leakage of the ionogel and the leakage-free behaviour of PEE are further verified in optical observation and composition analysis (Supplementary Fig. 26). Accordingly, the strain of the ionogel creeps from 44% to 54% (Supplementary Fig. 27). The signal also drifts in load–unload cycles (Fig. 3h) or in the case of superposed static and dynamic compression (Fig. 3i). The high stability of the PEE-based sensor is further verified under 10,000 cycles of load–unload with a peak pressure of 400 kPa (Supplementary Fig. 28a), whereas the control sensors using the (PVDF-HFP)–[EMIM][TFSI] ionogel (Supplementary Fig. 28b) or phosphoric acid (H$_3$PO$_4$)-doped poly(vinyl alcohol) (PVA) hydrogel generate drifting signals (Supplementary Figs. 28c and 29).
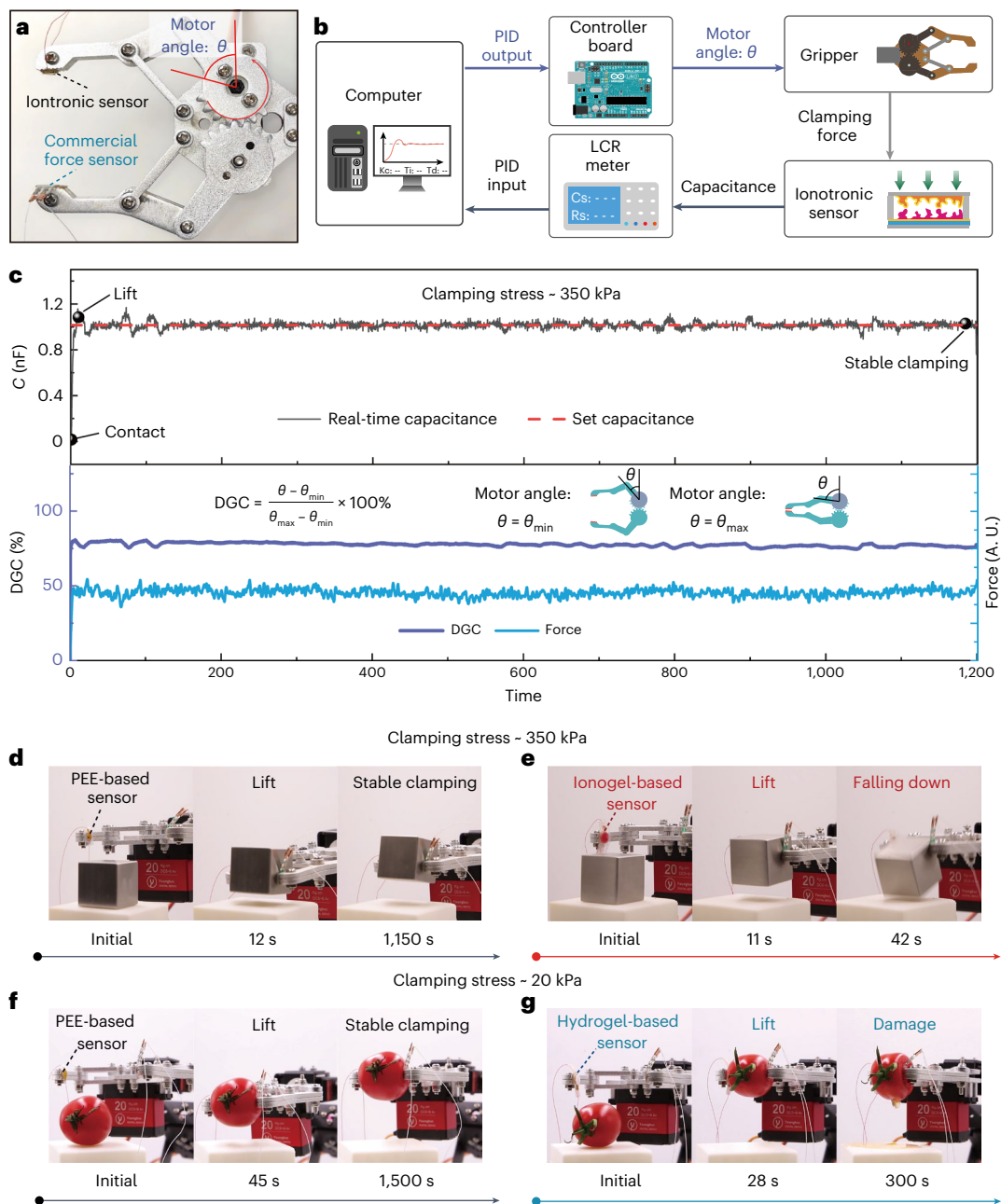
**Fig. 5 | Accurate force sensing for steady robotic manipulation. a**, Photo of a robotic gripper equipped with an iontronic sensor and a force sensor. **b**, Program diagram of the control system, containing a computer, a controller board, a gripper, an iontronic sensor and an LCR meter. **c**, Capacitance of the PEE-based sensor, DGC and force vary with time when clamping a steel block at a clamping stress of ~350 kPa. **d**, Sequential snapshots showing the stable control of the gripper with a PEE-based sensor for grasping a steel block. **e**, Sequential snapshots showing the unstable control of the gripper with an ionogel-based sensor for grasping the same steel block. **f**, Sequential snapshots showing the stable control of the gripper with a PEE-based sensor for grasping a cherry tomato at a clamping stress of ~20 kPa. **g**, Sequential snapshots showing the overload of the gripper with a hydrogel-based sensor for grasping a cherry tomato.

We propose to use two indices, drift ratio and drift rate, to quantitatively characterize the signal drift under static pressure. We assume that a sensor responds to a step stress and generates an initial capacitance $C_1$, and the signal gradually drifts to $C_2$ after a duration. The drift ratio is defined as the amount of capacitance drift $\Delta C$ (or $C_2 - C_1$) divided by the initial capacitance $C_1$, expressed as $\Delta C/C_1$ (Fig. 4a). The drift rate is defined as the tangent of capacitance normalized by $C_1$, $d(C/C_1)/dt$, and characterizes the rate of drift ratio over time.

Our sensor presents much lower drift compared with the iontronic sensors using ionogels, hydrogels or other solvent-free ionic elastomers in terms of drift ratio and drift rate. Figure 4b shows the

drift ratios of ten sensors, including our sensor, four sensors using ionogels ((PVDF-HFP)–[EMIM][TFSI] with different ionic liquid contents), one sensor using PVA–$H_3PO_4$ hydrogel, one sensor using the bis(trifluoromethane)sulfonimide lithium salt (Li[TFSI])-doped poly(n-butyl acrylate) elastomer and three sensors using conventional polyelectrolyte elastomers (PAMT with different crosslinker contents and P(AMT-co-AM)), tested under 500 kPa for 10 min. Our PEE-based sensors exhibit an average drift ratio of ~0.33% in 10 min, lower than those of all other sensors by two orders of magnitude. The drift ratio of the PEE-based sensor is lower than that of other sensors by two to four orders of magnitude (Supplementary Fig. 30). The drift ratio of

the PEE-based sensor becomes prominent at elevated pressures, for example, 3.8% under 700 kPa for 10 min (Supplementary Fig. 31). We thus conservatively set 500 kPa as the threshold for drift-free sensing. Also, the drift rate of the PEE-based sensor is smaller than that of other sensors by at least two to four orders of magnitude at 500 kPa (Fig. 4c). Although conventional polyelectrolyte elastomer-based sensors are leakage-free, their drift ratios (25.6–37.4% at 500 kPa for 10 min) are too high to allow accurate sensing. Therefore, the creep-free design of PEE is critical to eliminate signal drift.

Our sensor can work at a high pressure close to the Young's modulus of PEE without signal drift. Accurate sensing in traditional pressure sensors with hard materials can be achieved because the applied pressure is much smaller than the Young's modulus of the functional components such as silicon ($E \approx 100$ GPa). In flexible sensors, drift-free sensing is challenging due to the viscoelastic creep of soft materials, and drift-free sensing has been realized only under low pressures <10 kPa. We use a parameter, the pressure-to-modulus ratio ($P/E$), to characterize the allowable pressure that a sensor works without signal drift. Our sensor can work at a $P/E$ of 0.45 with an extremely low signal drift (<1%) over 10 min. By contrast, the sensors using conventional soft materials such as ionogels[13,30,35–37], hydrogels[31,38–40] or other ionic elastomers achieve drift-free sensing only at low $P/E$ ratios <$10^{-4}$, and the silicon-based sensors[41] allow a higher $P/E$ ratio of $10^{-3}$ but is still far lower than our result (Fig. 4d).

## Applications of the sensor for closed-loop robotic manipulation

Drift-free iontronic sensors are promising for applications of robotic manipulation to provide accurate sensing and feedback. We integrate the iontronic sensor with a robotic gripper (Fig. 5a), which is actuated by a motor and equipped with a commercial sensor for force monitoring. The actuation of the motor changes the gripping angle and the degree of gripper closure (DGC), defined as $(\theta - \theta_{\min})/(\theta_{\max} - \theta_{\min})$, where $\theta$, $\theta_{\min}$ and $\theta_{\max}$ are the real-time motor angle, minimum motor angle and maximum motor angle, respectively. We adopt a proportion integral differential (PID) program, which uses the signal of the sensor as the input and an Arduino board to control the system (Fig. 5b).

As a proof of concept, we demonstrate the accurate control of the gripper integrated with our sensor for stably gripping a steel block at a high clamping pressure of 350 kPa (Fig. 5c). Upon grasping, the capacitance increases. Once the set value of capacitance reaches, DGC is fixed and a command is sent to the gripper to lift the block. We show that the gripper can stably clamp the block for 20 min, during which both DGC and the clamping force remain stable (Supplementary Movie 1). The sequential snapshots of the stable control of the gripper are shown in Fig. 5d. By contrast, a control sensor using ionogel shows a drifting signal under a constant pressure of 350 kPa (Supplementary Fig. 32). The PID program keeps adjusting DGC to approach the capacitance to the set value, resulting in the slip-off of the steel block (Fig. 5e and Supplementary Movie 2).

The accurate detection of force of the PEE-based sensor enables the safe manipulation of fragile objects, such as a cherry tomato, as demonstrated by stably grasping a cherry tomato at 20 kPa (Supplementary Fig. 33) over 1,500 s (Fig. 5f and Supplementary Movie 3). By contrast, when an ionogel-based sensor is used, the up-drift of capacitance causes the decrease of DGC, and the cherry tomato slips off from the gripper (Supplementary Fig. 34 and Supplementary Movie 4). When a hydrogel-based sensor is used, the dehydration of the hydrogel induces a reduction in signal magnitude and an increase in DGC (Supplementary Fig. 35), which eventually crushes the cherry tomato (Fig. 5g and Supplementary Movie 5).

## Discussion

Previous efforts on flexible pressure sensors have mostly focused on improving sensing properties (for example, sensitivity[30], response time[40], working range[38], signal linearity[42] and operation bandwidth[43]), whereas the accuracy of transduction has been largely overlooked. For polymer-based sensors, signal drift is a common issue causing inaccurate measurement, specifically for applications under prolonged high pressures. This work shows that a rationally designed leakage-free and creep-free polyelectrolyte elastomer enables drift-free iontronic sensing.

The softness and the creep-free characteristics of PEE are balanced—short chains are often used in polymers to reduce creep but this increases the stiffness of the material. Our polyelectrolyte elastomer exhibits high softness ($E \approx 1.12$ MPa) and high toughness (~300 J m$^{-2}$) comparable with that of the commonly used PDMS elastomers. Low-creep elastomers have been studied, but these materials contain no ions[33,44]. When used as the dielectric layer, the sensors often exhibit low sensitivity. Our polyelectrolyte elastomer not only is creep-free but also exhibits higher sensitivity than that of conventional soft dielectric-based sensors.

The polyelectrolyte elastomer may find applications in reliable electrophysiological signal collection and strain sensing. The material is expected to be nontoxic because ions are trapped in the polymer network. By contrast, traditional ionogels can hardly be used to interface biological tissues and electrodes because of ion leakage[45]. The low-creep and low-hysteresis of PEE are also highly desired for strain sensing in both robotics and the human body because of the low residual deformation or delay in response.

## Online content

Any methods, additional references, Nature Portfolio reporting summaries, source data, extended data, supplementary information, acknowledgements, peer review information; details of author contributions and competing interests; and statements of data and code availability are available at https://doi.org/10.1038/s41563-024-01848-6.

## References

1. Luh, J., Fisher, W. & Paul, R. Joint torque control by a direct feedback for industrial robots. *IEEE Trans. Autom. Control* **28**, 153–161 (1983).
2. Cheng, G. et al. A comprehensive realization of robot skin: sensors, sensing, control, and applications. *Proc. IEEE* **107**, 2034–2051 (2019).
3. Dahiya, R. E-Skin: from humanoids to humans (point of view). *Proc. IEEE* **107**, 247–252 (2019).
4. Cho, A., Kim, J., Lee, S. & Kee, C. Wind estimation and airspeed calibration using a UAV with a single-antenna GPS receiver and pitot tube. *IEEE Trans. Aerosp. Electron. Syst.* **47**, 109–117 (2011).
5. Xu, Z. et al. Digital mapping of surface turbulence status and aerodynamic stall on wings of a flying aircraft. *Nat. Commun.* **14**, 2792 (2023).
6. Yang, S. et al. A survey of intelligent tires for tire-road interaction recognition toward autonomous vehicles. *IEEE Trans. Intell. Veh.* **7**, 520–532 (2022).
7. Liu, Y. et al. Electronic skin as wireless human–machine interfaces for robotic VR. *Sci. Adv.* **8**, eabl6700 (2022).
8. Zhu, M. L. et al. Haptic-feedback smart glove as a creative human–machine interface (HMI) for virtual/augmented reality applications. *Sci. Adv.* **6**, eaaz8693 (2020).
9. Sun, Z., Zhu, M., Shan, X. & Lee, C. Augmented tactile-perception and haptic-feedback rings as human–machine interfaces aiming for immersive interactions. *Nat. Commun.* **13**, 5224 (2022).
10. Chortos, A., Liu, J. & Bao, Z. Pursuing prosthetic electronic skin. *Nat. Mater.* **15**, 937–950 (2016).
11. Kang, S.-K. et al. Bioresorbable silicon electronic sensors for the brain. *Nature* **530**, 71–76 (2016).
12. Wang, L. et al. A review of wearable sensor systems to monitor plantar loading in the assessment of diabetic foot ulcers. *IEEE Trans. Biomed. Eng.* **67**, 1989–2004 (2020).

13. Su, Q. et al. A stretchable and strain-unperturbed pressure sensor for motion interference-free tactile monitoring on skins. *Sci. Adv.* **7**, eabi4563 (2021).

14. Lee, S. et al. Nanomesh pressure sensor for monitoring finger manipulation without sensory interference. *Science* **370**, 966–970 (2020).

15. Boutry, C. M. et al. A stretchable and biodegradable strain and pressure sensor for orthopaedic application. *Nat. Electron.* **1**, 314–321 (2018).

16. Yang, C. & Suo, Z. Hydrogel ionotronics. *Nat. Rev. Mater.* **3**, 125–142 (2018).

17. Chang, Y. et al. First decade of interfacial iontronic sensing: from droplet sensors to artificial skins. *Adv. Mater.* **33**, 2003464 (2021).

18. Lee, H. R., Kim, C. C. & Sun, J. Y. Stretchable ionics—a promising candidate for upcoming wearable devices. *Adv. Mater.* **30**, 1704403 (2018).

19. Yuan, Y. et al. Microstructured polyelectrolyte elastomer-based ionotronic sensors with high sensitivities and excellent stability for artificial skins. *Adv. Mater.* https://doi.org/10.1002/adma.202310429 (2023).

20. Sun, T. L. et al. Physical hydrogels composed of polyampholytes demonstrate high toughness and viscoelasticity. *Nat. Mater.* **12**, 932–937 (2013).

21. Leocmach, M., Perge, C., Divoux, T. & Manneville, S. Creep and fracture of a protein gel under stress. *Phys. Rev. Lett.* **113**, 038303 (2014).

22. Rubinstein, M. & Colby, R. H. *Polymer Physics* (Oxford Univ., 2003).

23. Biot, M. A. General theory of three-dimensional consolidation. *J. Appl. Phys.* **12**, 155–164 (1941).

24. Zhu, J. & Liu, Q. The osmocapillary effect on a rough gel surface. *J. Mech. Phys. Solids* **170**, 105124 (2023).

25. Karobi, S. N. et al. Creep behavior and delayed fracture of tough polyampholyte hydrogels by tensile test. *Macromolecules* **49**, 5630–5636 (2016).

26. Zhou, Y. et al. The stiffness-threshold conflict in polymer networks and a resolution. *J. Appl. Mech.* **87**, 031002 (2020).

27. Choi, J.-H., Xie, W., Gu, Y., Frisbie, C. D. & Lodge, T. P. Single ion conducting, polymerized ionic liquid triblock copolymer films: high capacitance electrolyte gates for *n*-type transistors. *ACS Appl. Mater. Interfaces* **7**, 7294–7302 (2015).

28. Kim, H. J., Chen, B., Suo, Z. & Hayward, R. C. Ionoelastomer junctions between polymer networks of fixed anions and cations. *Science* **367**, 773–776 (2020).

29. Fan, F. et al. Effect of molecular weight on the ion transport mechanism in polymerized ionic liquids. *Macromolecules* **49**, 4557–4570 (2016).

30. Yang, R. et al. Iontronic pressure sensor with high sensitivity over ultra-broad linear range enabled by laser-induced gradient micro-pyramids. *Nat. Commun.* **14**, 2907 (2023).

31. Bai, N. et al. Graded intrafillable architecture-based iontronic pressure sensor with ultra-broad-range high sensitivity. *Nat. Commun.* **11**, 209 (2020).

32. Zhang, Y. et al. Highly stable flexible pressure sensors with a quasi-homogeneous composition and interlinked interfaces. *Nat. Commun.* **13**, 1317 (2022).

33. Mannsfeld, S. C. B. et al. Highly sensitive flexible pressure sensors with microstructured rubber dielectric layers. *Nat. Mater.* **9**, 859–864 (2010).

34. Yiming, B. et al. A mechanically robust and versatile liquid-free ionic conductive elastomer. *Adv. Mater.* **33**, 2006111 (2021).

35. Nie, B., Li, R., Cao, J., Brandt, J. D. & Pan, T. Flexible transparent iontronic film for interfacial capacitive pressure sensing. *Adv. Mater.* **27**, 6055–6062 (2015).

36. Cui, X. et al. Flexible and breathable all-nanofiber iontronic pressure sensors with ultraviolet shielding and antibacterial performances for wearable electronics. *Nano Energy* **95**, 107022 (2022).

37. Yu, X. et al. Ultra-tough waterborne polyurethane-based graft-copolymerized piezoresistive composite designed for rehabilitation training monitoring pressure sensors. *Small* **19**, 2303095 (2023).

38. Bai, N. et al. Graded interlocks for iontronic pressure sensors with high sensitivity and high linearity over a broad range. *ACS Nano.* **16**, 4338–4347 (2022).

39. Li, P. et al. Skin-inspired large area iontronic pressure sensor with ultra-broad range and high sensitivity. *Nano Energy* **101**, 107571 (2022).

40. Shi, J. et al. Embedment of sensing elements for robust, highly sensitive, and cross-talk–free iontronic skins for robotics applications. *Sci. Adv.* **9**, eadf8831 (2023).

41. Terabe, H. et al. in *Proc. International Solid State Sensors and Actuators Conference (Transducers' 97)* Vol. 2 1481–1484 (IEEE, 1997).

42. Lu, P. et al. Iontronic pressure sensor with high sensitivity and linear response over a wide pressure range based on soft micropillared electrodes. *Sci. Bull.* **66**, 1091–1100 (2021).

43. Chen, X. et al. Channel-crack-designed suspended sensing membrane as a fully flexible vibration sensor with high sensitivity and dynamic range. *ACS Appl. Mater. Interfaces* **13**, 34637–34647 (2021).

44. Ha, K.-H. et al. Highly sensitive capacitive pressure sensors over a wide pressure range enabled by the hybrid responses of a highly porous nanocomposite. *Adv. Mater.* **33**, 2103320 (2021).

45. Docherty, K. M. & Kulpa, C. F. Jr Toxicity and antimicrobial activity of imidazolium and pyridinium ionic liquids. *Green. Chem.* **7**, 185–189 (2005).

## Methods

### Materials

The following chemicals 3-bromo-1-propanol (B108055), dichloromethane (DCM, D116144), acryloyl chloride (A104614), triethylamine (T103285), sodium sulfate anhydrous ($Na_2SO_4$, S112268), 1-methylimidazole (M109227), acetonitrile (A104443), 2,6-di-*tert*-butyl-4-methylphenol (D104365), ethyl acetate (EA, E116132), Li[TFSI] (B102576), 4-methoxyphenol (M104222), 1,6-hexanediol diacrylate (HDDA, H102721), 2-hydroxy-2-methylpropiophenone (1173, H110280), MA (M100030), *n*-butyl acrylate (B100035), 2,2'-azobisisobutyronitrile (A104256), [EMIM][TFSI] 99% and PVA (molecular weight ~145,000 g mol$^{-1}$) were purchased from Aladdin. PDMS (Sylgard 184) was purchased from Dow Corning, $H_3PO_4$, (≥85%) from Shanghai Macklin Biochemical and PI (28% in dimethylformamide) from DuPont. All chemicals were used as received without further treatment.

### Synthesis of AMT

To synthesize AMT, 35.05 g acryloyl chloride, 51.22 g 3-bromo-1-propanol and 44.79 g triethylamine were mixed in 600 ml DCM. After stirring at 0 °C overnight, the obtained 3-bromopropyl acrylate was washed with deionized (DI) water three times. The residual water was dried over $Na_2SO_4$, and DCM was removed via a rotary evaporator. Next, 29.69 g 3-bromopropyl acrylate, 18.92 g 1-methylimidazole and 0.2 g 2,6-di-*tert*-butyl-4-methylphenol were mixed in 100 ml acetonitrile and stirred in an $N_2$ atmosphere at 50 °C for 24 h. To purify 1-(3-(acryloyloxy)propyl)-3-methylimidazolium bromide, the mixture was thoroughly washed with EA (2,000 ml). After evaporating EA, 41.62 g Li[TFSI] and 450 ml DI water were mixed with 1-(3-(acryloyloxy)propyl)-3-methylimidazolium bromide and stirred overnight at room temperature. After ion exchange, AMT was extracted with 250 ml DCM and washed with DI water three times. The organic layer was then dried over $Na_2SO_4$, and DCM was evaporated at room temperature in a vacuum. Finally, 4-methoxyphenol was added as an inhibitor into the transparent light-yellow AMT. The final product was verified via NMR spectroscopy (Supplementary Fig. 1b,c). The yield was 42.37 g (24 wt.%).

### Synthesis of PEEs

A photo-initiator 1173 and crosslinker HDDA were mixed with AMT of 0.5 mol% and 3 mol%, respectively, with respect to the total amount of monomer, and the mixture was exposed to ultraviolet light (365 nm) for 3 h for the polymerization of PAMT. For the synthesis of P(AMT-co-MA), the synthetic procedure was the same as the above procedure except that both AMT and MA were used as monomers. For P(AMT-co-MA)-PMA, long-chain PMA was synthesized aforehand by mixing MA with 0.5 mol% of thermal initiator 2,2'-azobisisobutyronitrile at 65 °C under an $N_2$ atmosphere overnight and then added to the precursor of P(AMT-co-MA). After standing at room temperature for 2 days, the mixture was illuminated by ultraviolet light for 3 h and polymerized to form P(AMT-co-MA)-PMA.

### Synthesis of micro-structured PEE

The PVA solution, prepared by dissolving PVA powders in DI water at a mass ratio of 1:10 at 90 °C for 2 h, was poured on a commercial abrasive paper (no. 10000#) and dried for 12 h. The mould for PEE was made by sandwiching a 0.27-mm-thick PDMS (monomer-to-crosslinker ratio is 10:1) spacer between the abrasive-paper-templated PVA and a piece of glass. The PEE precursor was injected into the mould and cured under 365 nm ultraviolet light (30 W) for 3 h in an $N_2$ atmosphere. After curing, the sample was immersed in DI water for 30 min to separate PVA from the hydrophobic micro-structured PEE layer.

### Synthesis of micro-structured PVDF-HFP/[EMIM][TFSI] ionogel

One gram of PVDF-HFP was dissolved in 9 g acetone and stirred for 30 min at room temperature. Next, 3 g of [EMIM][TFSI] was added to the mixture and stirred for another 30 min at room temperature. The mixture was poured on the commercial abrasive paper (no. 10000#), left for 2 h at room temperature and heated at 40 °C for 2 h for acetone to evaporate. Finally, the micro-structured PVDF-HFP ionogel was peeled off from the abrasive paper.

### Synthesis of micro-structured PVA/$H_3PO_4$ hydrogel

Six grams of PVA were dissolved in 60 g DI water and stirred at 90 °C for 1 h. Next, 5 ml $H_3PO_4$ was added to the mixture and stirred at 60 °C for 1 h. The mixture was poured on the commercial abrasive paper (no. 10000#) and left at room temperature for 24 h. Finally, the micro-structured PVA/$H_3PO_4$ hydrogel was peeled off.

### Preparation of micro-structured PI–Au electrode and PET–Au electrode

For the PI–Au electrode, the precursor of PDMS (monomer-to-crosslinker weight ratio is 10:1) was poured on the commercial abrasive paper (no. 10000#) and cured at 60 °C for 24 h. The PDMS was peeled off, and the precursor of PI was spin-coated on the micro-structured surface of PDMS at 600 rpm for 1 min. The sample was heated stepwise from 40 °C to 240 °C and cooled down, both at an interval of 40 °C with a duration of 0.5 h. After being peeled off from PDMS, the micro-structured PI was sputter-coated with gold (25 mA for 300 s) and cut into a serpentine shape by laser cutting (CY-CT1NZ1-4030). For the PET–Au electrode, a PET film was sputter-coated with gold (200 nm) and cut into a serpentine shape.

### Fabrication of iontronic sensors

The micro-structured ionic conductor (PEE, PVDF-HFP/[EMIM][TFSI] or PVA/$H_3PO_4$) was cut into a circle (5 mm diameter) and sandwiched between the micro-structured PI–Au electrode and PET–Au electrode with a 50-µm-thick PDMS spacer. Finally, the sensor was packaged using two layers of 100-µm-thick PDMS. The initial capacitance of the sensor using PEE is ~1 pF.

### Mechanical characterizations of PEEs

All mechanical characterizations were performed using a mechanical testing machine Instron 68SC-1 with a 500 N load cell unless otherwise specified.

For the tensile test, the samples were cut into a rectangular shape, 30 mm in gauge length, 5 mm in width and 0.27 mm in thickness and glued to two acrylic plates before being clamped to the machine. The strain rate was 0.5 min$^{-1}$. The modulus was measured by linearly fitting the stress–strain curve in the strain range of 0–3%, and the work of fracture was calculated as the area underneath the stress–strain curve. For the loading and unloading tests, hysteresis was calculated by dividing the area enclosed by the loading and unloading curves by the area under the loading curve. For the creep test, or the static fatigue test, the sample was stretched stepwise to a stress of 200 kPa and maintained for 12 h. Two rectangular copper foils (5 × 5 mm$^2$) contacting the two ends of the sample were connected to an inductance, capacitance and resistance (LCR) meter to measure the impedance at a frequency of 10 kHz and a test voltage of 1 V. During the test, the displacement and impedance of the samples were continuously measured.

For toughness measurement, we used the pure shear test to measure the toughness of the samples[46]. Two sets of samples were prepared. One set had no pre-cut and the other set had an edge pre-cut of length 15 mm along the middle line of the samples. The samples were 3 mm long, 40 mm wide and 0.27 mm thick. The samples without pre-cut were stretched, and the stress–strain curves were recorded. The strain energy density at a certain strain ($\varepsilon$) is $W(\varepsilon)$. Next, the samples with pre-cut were stretched until the crack began to propagate at a critical

strain, $\varepsilon_c$. The toughness was calculated as $\Gamma = W(\varepsilon) \times H$, where $H = 3$ mm is the length of the samples at undeformed state.

For the compressive test, the samples were cut into a circular shape with 7 mm in diameter and 2 mm in height. A thin layer of lubricating oil was applied to the top and bottom surfaces of the sample to minimize the friction between the compression fixture and the sample. For monotonic compression, the loading velocity was 0.2 mm min$^{-1}$. For the fatigue test, the testing machine was Instron E3000 with a 250 N load cell with a force control mode applying triangular waves ranging from 0 to 400 kPa at a frequency of 1 Hz.

For the tack test, a 1-mm-thick smooth PEE layer was fixed to the loading stage using cyanoacrylate. The PI–Au film (15 mm diameter and 0.2 mm thickness) was attached to a cylinder acrylate and loaded to the testing machine. The PI–Au film was pushed downward to contact PEE at a pressure of 2 MPa for 5 min, and then pulled upward at 5 mm min$^{-1}$, during which the force–displacement curve was recorded. For the tack test of (PVDF-HFP)–[EMIM][TFSI] and PVA/H$_3$PO$_4$, the difference was that they used a microstructure with a thickness of 0.2 mm.

### Electrical characterizations of PEEs

The ac-impedance spectra were measured using 0.27-mm-thick circular samples of diameter 7 mm, using the impedance analyser Keysight E4990A with the 16334A fixture at an amplitude of 500 mV and within the frequency range of 20 Hz to 20 MHz. Before the test, the samples were sputter coated with gold (200 nm) on both sides. The total number of sampling points was 1,600. The data were fitted to the equivalent circuit model shown in the inset of Fig. 2i, and the results of PAMT and P(AMT-co-MA) are shown in Supplementary Fig. 15.

### Characterizations of iontronic sensors

The microstructures of the PVA template, PEE and PI–Au electrode were observed by scanning electron microscopy (TESCAN MIRA3). The capacitance values of different sensors were measured using an LCR meter (E4980AL, KEYSIGHT), and the response time was measured using another LCR meter that has a faster sampling rate (TH2840B). Cyclic compression of the sensors was performed using a mechanical testing machine (XLD-20E, Jingkong Mechanical Testing). Static compression was conducted by placing a 1 kg weight on the sensors for 10 min or 48 h. The sensors were connected to an LCR meter to monitor the variation of capacitance with time.

### Drift ratio and drift rate test

Weights of 100, 200, 300, 400, 500, 600, 700, 800, 900 and 1,000 g were placed on the sensors, which were equivalent to pressures of 50, 100, 150, 200, 250, 300, 350, 400, 450 and 500 kPa to the sensors. During compression, the capacitance of the sensor was continuously monitored for 10 min. For the sensor based on polybutyl acrylate (PBA)–Li[TFSI], the PBA-Li[TFSI] elastomer was synthesized by curing the precursor containing monomer $n$-butyl acrylate, 0.5 M Li[TFSI], 0.5 mol% initiator 1173 and 1 mol% crosslinker HDDA.

### Cyclic compressive test with square waves

The cyclic compressive test with square waves was programmed such that, during each cycle, the loading stage with a compression of 400 kPa lasted for 20 s, and the unloading stage lasted for 10 s. For the ionogels-based sensor, (PVDF-HFP)–[EMIM][TFSI] with a PVDF-HFP to [EMIM][TFSI] mass ratio of 1:2 was used. Force control mode was used to provide a loading rate of 400 kPa s$^{-1}$, while displacement control mode was used to provide an unloading rate of 5 mm s$^{-1}$.

### Superposition of static and dynamic compression

To apply a superposition of static and dynamic compression, the sensor was first loaded to a compressive stress of 400 kPa, and then, a sinusoidal compression with a frequency of 2 Hz was applied such that the pressure varied between 350 and 400 kPa.

### Response frequency test

To test the working frequency, the PEE-based sensor was loaded to cyclic loading and unloading with various frequencies by using a vibration generator (Model BL-ZDQ-2185, Hangzhou Peilin Instrument) up to 80 Hz. The signals were analysed using a fast Fourier transform.

### Manipulation of robotic grippers

A drift-free iontronic sensor and a commercial resistive force sensor (8 mm diameter and 0.2 mm thickness, maximum range 50 N) were fixed on the two fingers of a robotic gripper. A motor (Dongguan City Dsservo Technology, DS3218) was installed under the gripper for actuation. An LCR meter (TH2838A) was used to continuously measure the capacitance of the sensor using the Cs–Rs test mode with a medium testing speed at a test frequency of 10 kHz and a test voltage of 1 V. Using the PID control program provided by Labview (National Instruments), the real-time capacitance normalized by the set capacitance, and the normalized motor angle, DGC, was used as PID input and PID output, respectively. The PID output signal was transmitted to a controller board (Arduino UNO), which sent a pulse width modulation signal to control the rotation of the motor. At the same time, the voltage of the commercial sensor was measured and transmitted to the control board. The motor was also used to lift and lay down the gripper under the control of the Labview program. Because the motor angle could not be adjusted continuously, the real-time capacitance fluctuated slightly near the set capacitance.

### Reporting summary

Further information on research design is available in the Nature Portfolio Reporting Summary linked to this article.

## Data availability

The data that support the findings of this study are available at https://doi.org/10.6084/m9.figshare.25266307.

## References

46. Rivlin, R. & Thomas, A. G. Rupture of rubber. I. Characteristic energy for tearing. *J. Polym. Sci.* **10**, 291–318 (1953).

## Acknowledgements

## Author contributions

C.Y. and C.F.G. conceived the idea and designed the research. Y.H. designed, synthesized and characterized the polyelectrolyte elastomer. Y.C. designed, fabricated and characterized the drift-free iontronic sensor. Y.H. designed and performed the closed-loop robotic manipulation. C.Y. and C.F.G. drafted the manuscript. All authors discussed the results and commented on the manuscript.

## Competing interests

The authors declare no competing interests.

## Additional information

Corresponding author(s): Chuan Fei Guo

Last updated by author(s): Feb 20, 2024

# Reporting Summary

Nature Portfolio wishes to improve the reproducibility of the work that we publish. This form provides structure for consistency and transparency in reporting. For further information on Nature Portfolio policies, see our Editorial Policies and the Editorial Policy Checklist.

## Statistics

For all statistical analyses, confirm that the following items are present in the figure legend, table legend, main text, or Methods section.

| n/a | Confirmed | |
|---|---|---|
| ☐ | ☒ | The exact sample size ($n$) for each experimental group/condition, given as a discrete number and unit of measurement |
| ☒ | ☐ | A statement on whether measurements were taken from distinct samples or whether the same sample was measured repeatedly |
| ☒ | ☐ | The statistical test(s) used AND whether they are one- or two-sided *Only common tests should be described solely by name; describe more complex techniques in the Methods section.* |
| ☒ | ☐ | A description of all covariates tested |
| ☒ | ☐ | A description of any assumptions or corrections, such as tests of normality and adjustment for multiple comparisons |
| ☒ | ☐ | A full description of the statistical parameters including central tendency (e.g. means) or other basic estimates (e.g. regression coefficient) AND variation (e.g. standard deviation) or associated estimates of uncertainty (e.g. confidence intervals) |
| ☒ | ☐ | For null hypothesis testing, the test statistic (e.g. $F$, $t$, $r$) with confidence intervals, effect sizes, degrees of freedom and $P$ value noted *Give P values as exact values whenever suitable.* |
| ☒ | ☐ | For Bayesian analysis, information on the choice of priors and Markov chain Monte Carlo settings |
| ☒ | ☐ | For hierarchical and complex designs, identification of the appropriate level for tests and full reporting of outcomes |
| ☒ | ☐ | Estimates of effect sizes (e.g. Cohen's $d$, Pearson's $r$), indicating how they were calculated |

*Our web collection on statistics for biologists contains articles on many of the points above.*

## Software and code

Policy information about availability of computer code

| Data collection | The details about data collection are shown in the manuscript. |
|---|---|
| Data analysis | The details about data analysis are shown in the manuscript. |

For manuscripts utilizing custom algorithms or software that are central to the research but not yet described in published literature, software must be made available to editors and reviewers. We strongly encourage code deposition in a community repository (e.g. GitHub). See the Nature Portfolio guidelines for submitting code & software for further information.

## Data

Policy information about availability of data

All manuscripts must include a data availability statement. This statement should provide the following information, where applicable:
- Accession codes, unique identifiers, or web links for publicly available datasets
- A description of any restrictions on data availability
- For clinical datasets or third party data, please ensure that the statement adheres to our policy

All data needed to evaluate the study are presented in the main text or the supplementary information. The source data have been deposited into a public data repository and the DOI information has been shared. We declare no competing interests.

# Research involving human participants, their data, or biological material

Policy information about studies with human participants or human data. See also policy information about sex, gender (identity/presentation), and sexual orientation and race, ethnicity and racism.

| | |
|---|---|
| Reporting on sex and gender | N/A |
| Reporting on race, ethnicity, or other socially relevant groupings | N/A |
| Population characteristics | N/A |
| Recruitment | N/A |
| Ethics oversight | N/A |

Note that full information on the approval of the study protocol must also be provided in the manuscript.

# Field-specific reporting

Please select the one below that is the best fit for your research. If you are not sure, read the appropriate sections before making your selection.

☒ Life sciences ☐ Behavioural & social sciences ☐ Ecological, evolutionary & environmental sciences

For a reference copy of the document with all sections, see nature.com/documents/nr-reporting-summary-flat.pdf

# Life sciences study design

All studies must disclose on these points even when the disclosure is negative.

| | |
|---|---|
| Sample size | N/A |
| Data exclusions | No data exclusion involved. |
| Replication | N/A |
| Randomization | N/A |
| Blinding | N/A |

# Reporting for specific materials, systems and methods

We require information from authors about some types of materials, experimental systems and methods used in many studies. Here, indicate whether each material, system or method listed is relevant to your study. If you are not sure if a list item applies to your research, read the appropriate section before selecting a response.

## Materials & experimental systems

| n/a | Involved in the study |
|---|---|
| ☒ | Antibodies |
| ☒ | Eukaryotic cell lines |
| ☒ | Palaeontology and archaeology |
| ☒ | Animals and other organisms |
| ☒ | Clinical data |
| ☒ | Dual use research of concern |
| ☒ | Plants |

## Methods

| n/a | Involved in the study |
|---|---|
| ☒ | ChIP-seq |
| ☒ | Flow cytometry |
| ☒ | MRI-based neuroimaging |

## Plants

| | |
|---|---|
| Seed stocks | N/A |
| Novel plant genotypes | N/A |
| Authentication | N/A |